

Shape Back-Projection In 3D Scenes

Ashish Kumar¹, L. Behera¹, *Senior Member IEEE*, K. S. Venkatesh¹

{<https://github.com/ashishkumar822>}

Abstract—In this work, we propose a novel framework shape back-projection for computationally efficient point cloud processing in a probabilistic manner. The primary component of the technique is shape histogram and a back-projection procedure. The technique measures similarity between 3D surfaces, by analyzing their geometrical properties. It is analogous to color back-projection which measures similarity between images, simply by looking at their color distributions. In the overall process, first, shape histogram of a sample surface (e.g. planar) is computed, which captures the profile of surface normals around a point in form of a probability distribution. Later, the histogram is back-projected onto a test surface and a likelihood score is obtained. The score depicts that how likely a point in the test surface behaves similar to the sample surface, geometrically. Shape back-projection finds its application in binary surface classification, high curvature edge detection in unorganized point cloud, automated point cloud labeling for 3D-CNNs (convolutional neural network) etc. The algorithm can also be used for real-time robotic operations such as autonomous object picking in warehouse automation, ground plane extraction for autonomous vehicles and can be deployed easily on computationally limited platforms (UAVs).

I. INTRODUCTION

Accurate depth sensing and its efficient processing is crucial for a robotic system to reliably perform tasks such as object pick, place or autonomous navigation. The depth data is acquired by the depth sensors and is commonly known as point clouds. The current depth sensors can provide millions of point cloud data in near real time. However, processing them, in general, requires huge computing power. Hence, driven by the significance of the depth information, in this paper, we focus on exploring local geometrical properties of a point cloud such that multiple tasks in the area of 3D perception can be reasoned by computing only once.

Typically, a point cloud is either organized or unorganized. An organized cloud is represented as a 2D matrix in which each location corresponds to a 3D point similar to a pixel in an image. Such clouds offers straightforward use of the 2D image processing techniques (e.g. edge detection) and facilitates fast nearest neighbor computations. On the other hand, unorganized clouds are simply a collection of 3D points which does not convey any spatial or structural connectivity. These clouds are often represented in form of kD-trees [1] or Octrees [2] which facilitate efficient (but slower than organized) nearest neighbor search [3] as well as reduced memory storage. Most common sources of organized point cloud are stereo cameras, Time-of-Flight

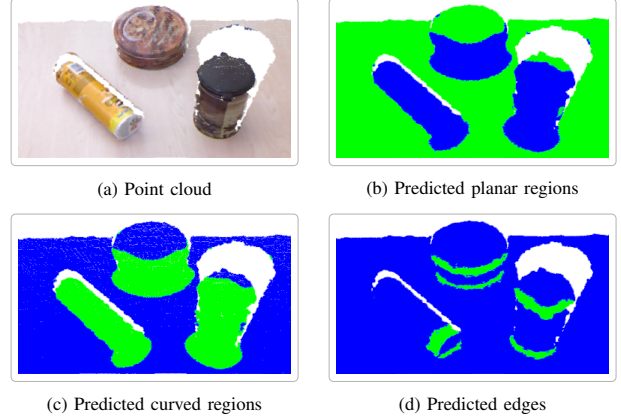


Fig. 1: Output of the algorithm for tasks such as plane segmentation, curved region segmentation, and edge detection.

cameras such as Microsoft Kinect, Intel real sense, IDS-Ensenso etc. Whereas, the LIDAR [4] sensors are a major source of unorganized point clouds. Due to long range and high accuracy, they are preferred in autonomous driving and navigation [5], [6], warehouse automation, robotic object manipulation and other industrial applications.

In order to advance the state-of-art in the above areas, several worldwide robotic challenges have been hosted previously such as Amazon Picking Challenge, 2015 and 2016, Amazon Robotics Challenge, 2017 for warehouse automation, MBZIRC, DARPA humanoid [7] and autonomous driving [8] challenges. Interestingly, all of them have a large technological overlap between them which primarily includes object detection and segmentation of images and point clouds, edge detection (2D or 3D), object pose estimation, 3D model fitting for robot grasping.

The state-of-art (SOA) algorithms for object detection [9], [10], [11], [12], [13], [14], [15] in images are based on Convolutional Neural Network (CNN) architectures [16], [17], [18]. The CNNs have also been employed in 3D perception, such as point cloud segmentation [19], semantic 3D scene completion [20], and 3D object segmentation [21]. These variants of CNNs are known as 3D-CNNs. The 3D-CNNs require huge amount of labeled point cloud data which comes at a cost of specialized softwares and exhaustive manual efforts. Despite the accuracies, their computational and memory intensive nature limits their scope for real time applications [22], [23] on limited computing platforms such as Unmanned Aerial Vehicles (UAVs).

As an alternative, traditional feature matching [24], [25]

¹Mr. Ashish Kumar, Dr. L. Behera and Dr. K. S. Venkatesh are with the Department of Electrical Engineering, Indian Institute of Technology, Kanpur {krashish, lbehera, venkats}@iitk.ac.in

and consensus based model fitting [26] methods are preferred. The former involve computing of handcrafted features based on local geometrical information of a model point cloud and matching them with the features computed for a target point cloud. The feature matching procedure is a compute intensive task and its performance is severely deteriorated even for minor 3D surface variations between the model and the target. Inconsistent depth data is the primary reason for this which often results in inaccurate feature estimation and matching.

On the other hand, the consensus based methods of RANSAC [27], LMeds [28] are a primary choice to fit primitive shapes (e.g. plane, cylinder or sphere) into point clouds. These methods perform iterative random sampling of the input points and estimates model parameters (plane coefficients, cylinder or sphere radii). However, sampling and the estimation process becomes computationally inefficient when a large number of points are irrelevant to the model to be fit. In case of multiple model instances, the algorithm is iterated exactly equal to number of instances, which in some applications, is not known beforehand. Moreover, their capabilities to only deal with primitive shapes, limit their applicability in real world scenarios, because many objects are often complex shaped, i.e. neither a plane nor a cylinder.

Furthermore, robust edge detection in the point clouds is quite important for various robotic applications. It can be achieved in the organized point clouds (depth images) simply by using the techniques of edge detection in RGB images. Whereas, unorganized cloud needs special treatment. Such cases are generally occurs when a raw organized point cloud undergoes noise removal preprocessing operations and loses its spatial and structural connectivity (unorganized cloud). Sometimes, the depth sensors (LIDARs) directly provides unorganized point cloud data. Due to the lost spatial relations, edge detection in unorganized point clouds becomes quite challenging and have gained only a little attention [29]. The approach is based on Eigen value analysis with all results reported only for synthetic data.

In this paper, we propose a novel probabilistic framework *Shape Back-projection* which addresses all of the above limitations in a non-iterative manner. The most crucial part of the algorithm is shape histograms which encodes the 3D information in such a way that it can be utilized for a number of applications while avoiding complex computations. We experimentally demonstrate that, shape back-projection can be deployed independently for the tasks of point cloud classification, edge detection, especially in the unorganized clouds. Unlike consensus based methods, the proposed algorithm can deal with any number of instances, without manual specification. The algorithm also outperforms a recent algorithm [29] of edge detection in unorganized point clouds. Moreover, the algorithm can also be effective to facilitate automated labeling of 3D point cloud data, required for 3D-CNNs

In the following sections, first, we lay a preliminary ground on which the whole idea is based (Sec. II). Then, we discuss core of the algorithm (Sec. III). At the end, we report

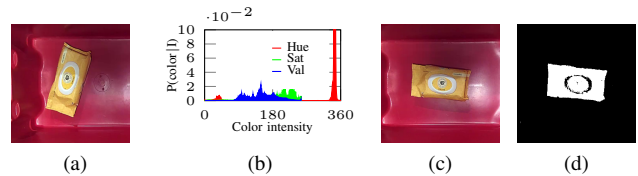


Fig. 2: (a) Sample image, (b) corresponding HSV histogram, (c) test image, and (d) back-projection of the hue histogram of the object pixels in the sample image onto the test image.

comprehensive experimental analysis (Sec.IV) and discuss the primary applications of shape back-projection.

II. PRELIMINARIES

A. Color Histograms

Color histogram is a discretization of a color space such as (Red, Green, Blue), (Hue, Saturation, Value), etc and represents a frequency distribution over the pixel colors in an image. Each component of a color space is referred as a channel. Let C be a k -bin color histogram to be computed over a single color channel. First, a *bin-id* (Eq. 1) for a pixel is obtained and the corresponding bin value is incremented by one. This process is repeated for all or only a desired set of pixels. The obtained frequency distribution (C) is then normalized (C_n) with the number of pixels which participated in the histogram computation. The normalization step essentially scales all the bin values to sum them up-to one so that it can follow the properties of a valid probability density function. Fig. 2b shows single channel normalized histograms of H, S, V components of a sample image (Fig. 2a).

$$bin-id = \left\lfloor \frac{color}{k} \right\rfloor \quad (1)$$

B. Color Back-projection

Back-projection [30] is a technique to identify test data patterns, behaving almost similar to that of a given distribution. In the context of images, color histograms are back-projected to localize color patterns similar to a given color histogram. In the first step of back-projection, normalized color histogram of the pixels of interest in a sample image is computed (object pixels in Fig. 2a). Later, for each pixel in a test image (Fig. 2c), *bin-id* is obtained and assigned a score (Eq. 2) equal to the value of bin-id in the color histogram. The score is referred as back-projection likelihood which depicts that how likely a pixel in the test image belongs to the object in the sample image.

$$P(pixel = color | C_n) = C_n(bin-id) \quad (2)$$

In general, hue component of the HSV color space is preferred for color back-projection because it carries the chrominance information about a pixel-color. However, the selection of color component may vary from application to application. Color back-projection has been explored previously in various applications such as real time object tracking in images using Mean-Shift [31], Cam-Shift [32].

III. SHAPE BACK-PROJECTION

Shape back-projection is inspired by color back-projection and comprises of shape-histogram analogous to a color histogram. By back-projecting the shape histograms onto 3D surfaces, points of a particular interest can be obtained in a probabilistic manner, similar to obtaining pixels of interest in the color back-projection process.

A. Shape Histograms

A shape histogram has been designed by carefully observing the geometrical properties of 3D surfaces such as normals, and curvature. To understand this, consider a planar and a curved surface (S) as shown in Fig. 3a and 3c. Let $p_i, p_j \in S$ be a point and its neighbor respectively and n_i, n_j be their normals. For each (p_i, p_j) pair, we define an angle α_{ij} between n_i and n_j . An individual α_{ij} does not convey much information, however, the α_{ij} s for all neighbors of p_i governs the behavior of local surface variations around p_i . By the visual inspection of Fig.3b and 3d, it can be inferred that larger the α , more is the surface curved around p_i . Based on this fact, we exploit the information contained in the α_{ij} s which we call *Inter Normal Angle Difference* (INAD). We parameterize INAD as a mean and standard deviation (μ, σ) value pair of the α_{ij} s for each p_i . The INAD pair essentially captures a Gaussian distribution $\mathcal{N}(\mu, \sigma^2)$ of curvature around p_i which is given by Eq.3, 4.

$$\mu_i = \frac{1}{N} \sum_{j=1}^N \alpha_{ij} \quad (3)$$

$$\sigma_i = \sqrt{\frac{1}{N} \sum_{j=1}^N (\alpha_{ij} - \mu_i)^2} \quad (4)$$

Further, in order to obtain the shape histogram of a given surface, firstly, INAD for each $p_i \in S$ is computed. Later, a cumulative distribution of these INAD pairs is obtained in a way similar to that of color histogram computation. It is important to note that the INAD is composed of two values: μ, σ . Thus, a shape histogram is simply two dimensional and to accommodate this, the Eq.1 can be rewritten as Eq.5, where, k_μ, k_σ are the number of bins in the μ and σ axis

$$bin-id_{\mu_i} = \left\lfloor \frac{\mu_i}{k_\mu} \right\rfloor, \quad bin-id_{\sigma_i} = \left\lfloor \frac{\sigma_i}{k_\sigma} \right\rfloor \quad (5)$$

Next, the obtained cumulative distribution is normalized by dividing it with the maximum value in the distribution. The normalized cumulative distribution is termed as a shape-histogram. Fig.3e-3h depicts the shape histogram of a synthetically generated planar and a curved surface for different values of neighborhood search radii r .

The INAD computations are entirely based on surface normals. Therefore, noisy normals can severely affect the shape histograms. Most of the noise comes directly from the depth sensors which is aggregated with the approximate solutions errors, introduced by the normal estimation process. Hence, it becomes necessary to deal with the case of noisy normals. Ideally, it would be impossible to obtain 100%

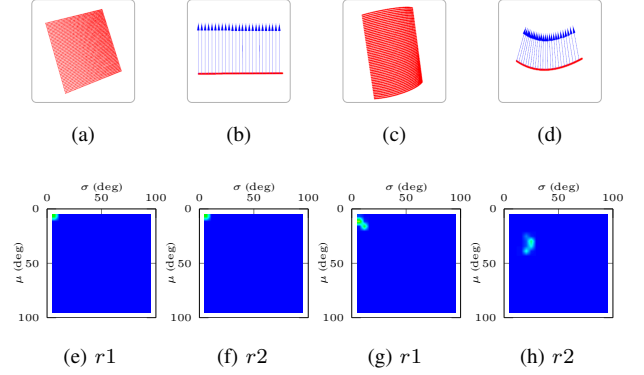


Fig. 3: (a), (c) Sample planar and curved surfaces. (b), (d) corresponding profile of surface normals, points (red) and normals(blue). (e), (f) shape histograms of planar surface, and (g), (h) curved surface for different values of neighborhood search radii $r1$ and $r2$, where $r1 < r2$ Higher green, higher probability.

noise free normals. Thus, we employ a noise cancellation procedure based on simple statistical outlier removal technique. Before discussing the noise cancellation procedure, we briefly introduce the normal estimation process below.

1) **Normal Estimation:** Let p_i be any point in \mathbb{R}^3 and $N \subset S$ be the set of all neighboring points around P in a spherical region of radii r . A covariance matrix (\mathcal{C}) in \mathbb{R}^3 is computed from a point set $P \cup N$ and decomposed into Eigen vectors. The matrix \mathcal{C} essentially captures the spatial behavior (variance or spread) of neighboring points around p_i and an Eigen vector quantifies both the direction and amount of spread. In general, a surface has minimal spread in a direction normal to it. Therefore, the Eigen vector having lowest Eigen value can be taken as an approximation to the normal at p_i . The above methodology is the most simple and fastest approximation of normals and its practical implementations are publicly available in the Point Cloud Library (PCL) [33].

2) **Noise Removal:** After the normal estimation process, α_{ij} s for each p_i are computed using inverse cosine rule¹. At this stage, we assume that some of the α_{ij} s may be noisy. To filter such values, we perform statistical outlier rejection operation on α_{ij} s. This step eliminates noisy normals up-to a great extent, leading to consistent normals in the output. The mathematical treatment of the operation is given by Eq. (3, 4, 6). Here, c is referred as an outlier rate which controls the number of outliers in the output. Decision for a point to be an outlier or inlier is given by Eq. 6.

$$p_j \text{ is } = \begin{cases} \text{Inlier}, & \text{if } \frac{|\alpha_{ij} - \mu_i|}{\sigma_i} \leq c \\ \text{Outlier}, & \text{Otherwise} \end{cases} \quad (6)$$

The filtered α_{ij} s are now plugged into Eq. 3, 4 in order

¹ $\alpha_{ij} = \cos^{-1}\left(\frac{n_i \cdot n_j}{|n_i| \cdot |n_j|}\right)$

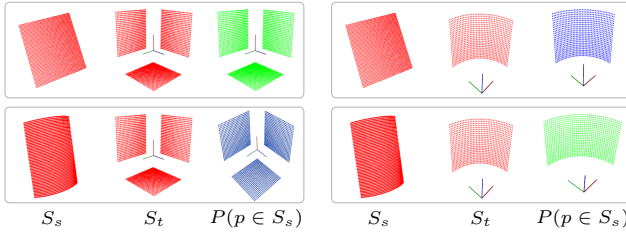


Fig. 4: Shape back-projection for various S_s - S_t pair

to compute the new values of μ_i and σ_i which collectively represents INAD at p_i . It must be noted that any point $p_j \in N$ marked as an outlier is not included into computation of μ_i and σ_i . Fig. 3e and 3g shows shape histogram computed for a planar and a curved surface.

B. Shape Histogram Back-projection

Shape histogram back-projection is functionally analogous to the color histogram back-projection. In this case, the back-projection likelihood score depicts that: “how likely a point in a test surface is following geometrical properties similar to that of represented by the shape histogram of a sample surface”. The mathematical expression for such a likelihood is given in Eq.7, where S_s and SH refers to a sample surface and its shape histogram respectively.

$$P(p_i \in S_s | SH, r) = SH(bin-id_{\mu_i}, bin-id_{\sigma_i}) \quad (7)$$

In order to back-project a shape histogram, first the INAD for each point in a test surface S_t is computed (Eq.3, 4). The INAD is then used to obtain $bin-id_{\mu}$ and $bin-id_{\sigma}$ which are then plugged into Eq.7 to obtain the likelihood.

Fig.4 shows examples of the shape back-projection procedure. The column-1 represents the case when shape histograms of a planar and a curved surface (S_s) are back-projected onto a test surface (S_t), having three orthogonal planes. It can be noticed that the likelihood obtained is higher (●) when both S_s and S_t belong to similar kind of surfaces (planar-planar). Whereas, it is lower (●) when S_s and S_t are of different kinds (curved-planar). Similarly, the column-2 represents the case when shape histogram of the planar and curved sample surfaces is back-projected onto a curved test surface S_t .

In the performance of shape back-projection, the neighborhood search radii r is a crucial parameter. The variations in the values of r lead to different utilities of shape back-projection, which we have experimentally demonstrated in the following section.

IV. EXPERIMENTS

In this section, we provide quantitative and qualitative results of Shape Back-projection. The experimental evaluation is done by varying the values of parameters such as number of histograms bins (k), neighbor search radii (r). In order to evaluate the algorithm against noise and demonstrate its real world usefulness, we choose publicly available point cloud dataset [33] containing 108 organized point clouds,

acquired by Microsoft Kinect sensor. Each cloud contains a clutter of household objects placed on top of a table. The clouds are deliberately converted into unorganized format. Due to the unavailability of ground truths for the purpose of binary surface classification and edge detection, we manually generate them using CloudCompare [34]. All the experiments are performed only on a i7-6850-K CPU and 64GB RAM. It must be noticed that shape-histograms does not represent any feature e.g.[24], [25], therefore we have limited our discussion only to variations in hyper-parameters of shape-histograms and its utilities.

A. Varying “r”

The INAD score for a point depends on the number of the spatial neighbors, which in turn is governed by r . Fig. 3e-3h shows shape histograms of Fig. 3a and 3c for varying r . It can be seen that as r is increased, the peak in the shape histogram of a planer surface doesn’t change whereas it shifts towards higher bins for the case of a curved surface. Thus, we make an important observation that the value of r essentially captures the information about the curvature at a point. We exploit the observation and show that by computing shape histogram of a surface only once, we can use it for different purposes as given below.

1) **Binary Surface Classification:** Surface segmentation is a most fundamental operation which is required in order to segregate points with similar geometrical properties into different clusters. In this direction, the learning based [21], [19] approaches exists, however, they require tremendous amounts of data and GPUs for their operations. Here, we demonstrate that shape back-projection can achieve high accuracies for binary surface classification merely on a CPU.

The 3D surfaces can be broadly classified into two categories i.e. planar and curved (non-planar). We can say that if a point is more likely to be on a planar surface, it will be less likely to be on a curved surface and vice-versa. Therefore if we have shape histogram of a planar surface, the Eq. 8 holds.

$$P(p \in S_{plane}|SH, r) + P(p \in S_{curved}|SH, r) = 1 \quad (8)$$

To verify this, we compute shape histogram of a planar surface and back-project onto the real 3D scenes as shown in column-(1) Fig. 5. Corresponding color coded likelihoods $P(p \in S_{plane}|SH, r)$ and $P(p \in S_{curved}|SH, r)$ are shown in column-(2,3) Fig. 5. The likelihood score proves the validity of Eq. 8 qualitatively. The Table I depicts the precision, recall, F1 and mIoU [35] scores to assess the binary classification quality. These values are heavily dependent on the quality of the ground truth which we have manually generated. The planar class have high precision and high recall values. Whereas, high recall and relatively low precision for curved surfaces can be accounted by the misclassification of planar points as well as inaccurate ground truths near the high curvature edges. Despite the relatively low precisions for the curved surfaces, the qualitative analysis of binary classification (Fig. 5 column-2-5) is quite pleasant.

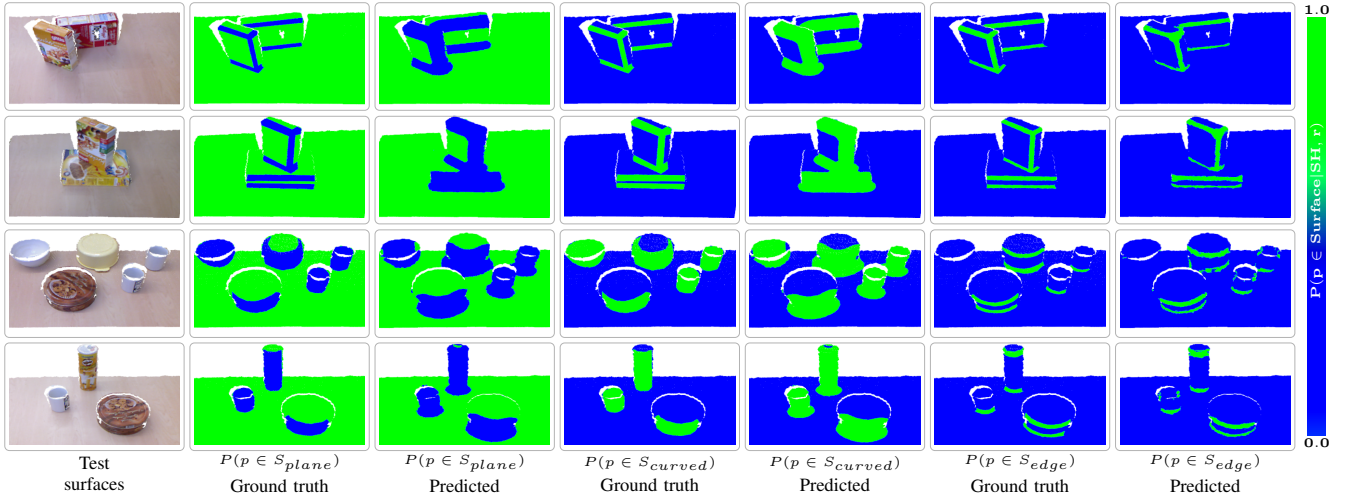


Fig. 5: Qualitative results of shape back-projection for binary surface classification and edge detection

2) **Edge Detection in Unorganized Point Clouds:** We target this task as a utility of shape back-projection by employing two facts: first, the INAD captures the amount of curvature at a point and second, the edges have high curvature as compared to a plane. Therefore, we reduce r to a smaller value ($\sim 6mm$) and then back-project the shape histogram of a planar surface onto the 3D scenes as shown in column-1 Fig. 5. Since, the edges are also curved regions in a cloud, therefore, the Eq. 8 can be rewritten as given below.

$$P(p \in S_{plane}|SH, r) + P(p \in S_{edge}|SH, r) = 1 \quad (9)$$

Table II shows the precision, recall and the F1-Score for edge detection using shape back-projection and a recent method [29]. It can be inferred that the recent method performs well for synthetic data which they have reported in their paper, however, performs quite inferior on real data. This is where, the shape back-projection marks its importance to reliably deal with real data. Fig. 5 column-(6-7) shows the color coded edge likelihood $P(p \in S_{edge}|SH, r)$ corresponding to the clouds in column-(1). It can be seen that the predicted edges appears quite similar to the ground truth.

B. Number of Bins (k_μ, k_σ) and its Effect on Noise

To study the effect of noise, we don't rely on adding noise in the synthetic point clouds as performed in [29], instead the chosen point clouds fulfills the purpose, as they are full of random noise and inconsistency depth measurements. Table II depicts the precision, recall and F1 measure for high curvature edge detection in the real point clouds data well as a synthetic cloud (Fig. 6). It is noticeable that the best F1 (in blue) on real data is obtained with higher number of bins while for the synthetic point cloud, it is achieved with lower number of bins. It happens because noisy point cloud contains local surface variations which can not be represented for small values of k . On the other hand, high values of k accurately encodes such information and does not

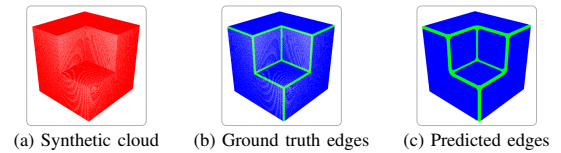


Fig. 6: Edge detection in synthetic unorganized point cloud

let the noise hamper the underlying geometrical information. Hence, the shape histograms inherently deals with surface noise which is desirable for many practical applications.

C. Timing Analysis and Point Cloud Density

The INAD score heavily relies on number of nearest neighbors (k -NNs) which depends on the cloud density. In general, the real point cloud data is noisy and poses non-uniform density. Therefore, rather changing the radii, timing analysis is performed by explicitly varying the number of nearest neighbors in a synthetic point cloud (Fig. 6). Table III shows the INAD computing performance for a single point with different number of nearest neighbors. On a scale, 10 and 500 neighbors roughly corresponds to a radii of 0.005m and 0.03m on surface of resolution 0.001m. The method is quite fast even on single thread. This enables shape back-projection to be deployed on computationally limited platforms. The speeds can be increased several times by taking advantage of multi-threading and GPUs, if available.

D. Rotation and Translation Invariancy

Shape back-projection exploits local geometrical properties. In this process, the INAD score for a point is computed using surface normals which are in turn computed locally and invariant to 3D affine transformation. Therefore, the INAD score and the shape histograms remain rotational and translational invariant.



Fig. 7: Our robotic setup performing an autonomous picking operation on the grasp location provided by shape back-projection.

E. A Promising Alternative to Model Consensus

Consider the point cloud in the Fig.5 row-3. In order to extract all the cylindrical items from the cloud, model consensus needs to be deployed iteratively and number of cylinders (instances) must be known beforehand. On the other hand, binary surface classification using shape back-projection can classify all instances without requiring to have the total number of instances apriori and can also deal with variety of shapes, unlike model consensus which are primitive only. Table IV shows the precision, recall and F1-score of shape back-projection and RANSAC to extract all cylinders in the the the cloud-Id 33 (Fig.5, row-3).

V. PRACTICAL APPLICATIONS

1) **Warehouse Automation:** A large number of novel items arrive in the warehouses on a daily basis. Dealing with such items becomes a major challenge because not every item can be included in the dataset of the learning based perception algorithms. In such cases, the binary surface classification using shape back-projection can be utilized in order to segregate items in the cluttered containers on the basis of their 3D shape and the segregated items then can be sent to different destinations for further processing.

2) **Suction Grasp Location Estimation:** Through our participation in the Amazon challenges APC'16 and ARC'17, we have realized that the centroid based approach [36] is not suitable for suction based grasping in the presence of partial occlusions, and especially when a smaller object lies on top of a larger object. As a solution, shape-histogram of a planar or curved surface (depending on the target object shape) is back-projected onto the point cloud of a target object. Then, an adaptive mean-shift operation is performed on the back-projection likelihood and its convergence point is chosen as the suction grasp location (Fig. 7). This strategy is quite fast, effective and also eliminates a need of time consuming 6D pose estimation such as Super4PCS [37].

3) **Automated data labeling for 3D-CNNs:** In order to train 3D-CNNs for the task of surface classification, a huge amount of data is required. Manual labeling of 3D point clouds is quite exhaustive and challenging as compared to images and requires specialized softwares. Hence, shape back-projection can be deployed to segment specific kind of surfaces from a 3D scene and its output can be used to generate ground truths. For example, the outputs of algorithm

in Fig.4 can be used to generate dataset to train a 3D CNN for purpose of surface segmentation and to detect edges.

VI. CONCLUSION

In this work, we have presented a novel algorithm of shape back-projection in 3D scenes. Its inspiration lies in the working of color back-projection which obtains color similarity between two images by analyzing their color histograms. Here, we have developed a novel shape histogram, by means of which, a probabilistic measure of similarity between two 3D point clouds can be obtained. The utility of the shape back-projection ranges from warehouse automation to automated labeled data generation for 3D-CNNs. The existing feature based 3D object detection methods can also be benefitted by extracting salient points using shape back-projection. The algorithm is a robust and a computationally efficient alternative to the SOA algorithms for the above purposes. Therefore, it can be easily deployed on computationally limited platforms (UAVs) for complex tasks of object manipulation.

REFERENCES

- [1] J. L. Bentley, "Multidimensional binary search trees used for associative searching," *Communications of the ACM*, vol. 18, no. 9, pp. 509–517, 1975.
- [2] D. J. Meagher, *Octree encoding: A new technique for the representation, manipulation and display of arbitrary 3-d objects by computer*. Electrical and Systems Engineering Department Rensselaer Polytechnic Institute Image Processing Laboratory, 1980.
- [3] M. Muja and D. G. Lowe, "Flann, fast library for approximate nearest neighbors," in *International Conference on Computer Vision Theory and Applications (VISAPP'09)*, vol. 3, INSTICC Press, 2009.
- [4] Velodyne, "Velodyne HDL-64E: A high definition LIDAR sensor for 3D applications," tech. rep., Velodyne, October 2007. Available at www.velodyne.com/lidar/products/white.paper.
- [5] D. Lavrinc, "Ford unveils its first autonomous vehicle prototype <http://www.wired.com/autopia/2013/12/ford-fusion-hybrid-autonomous>," *Accessed December 16th*, 2013.
- [6] E. Ackerman, "Tesla model S: Summer software update will enable autonomous driving," *IEEE Spectrum Cars That Think*, 2015.
- [7] G. Pratt and J. Manzo, "The darpa robotics challenge [competitions]," *IEEE Robotics & Automation Magazine*, vol. 20, no. 2, pp. 10–12, 2013.
- [8] M. Buehler, K. Iagnemma, and S. Singh, *The DARPA urban challenge: autonomous vehicles in city traffic*, vol. 56. springer, 2009.
- [9] C. Zhu, Y. Zheng, K. Luu, and M. Savvides, "Cms-rnn: contextual multi-scale region-based cnn for unconstrained face detection," in *Deep Learning for Biometrics*, pp. 57–79, Springer, 2017.
- [10] R. Girshick, "Fast r-cnn," in *Proceedings of the IEEE international conference on computer vision*, pp. 1440–1448, 2015.
- [11] S. Ren, K. He, R. Girshick, and J. Sun, "Faster r-cnn: Towards real-time object detection with region proposal networks," in *Advances in neural information processing systems*, pp. 91–99, 2015.
- [12] J. Long, E. Shelhamer, and T. Darrell, "Fully convolutional networks for semantic segmentation," in *Proceedings of the IEEE Conference on Computer Vision and Pattern Recognition*, pp. 3431–3440, 2015.
- [13] H. Zhao, J. Shi, X. Qi, X. Wang, and J. Jia, "Pyramid scene parsing network," in *Proceedings of IEEE Conference on Computer Vision and Pattern Recognition (CVPR)*, 2017.
- [14] K. He, G. Gkioxari, P. Dollár, and R. Girshick, "Mask r-cnn," *CVPR*, 2017.
- [15] G. Lin, A. Milan, C. Shen, and I. D. Reid, "Refinenet: Multi-path refinement networks for high-resolution semantic segmentation," in *Cvpr*, vol. 1, p. 5, 2017.
- [16] K. He, X. Zhang, S. Ren, and J. Sun, "Deep residual learning for image recognition," in *Proceedings of the IEEE conference on computer vision and pattern recognition*, pp. 770–778, 2016.
- [17] G. Huang, Z. Liu, K. Q. Weinberger, and L. van der Maaten, "Densely connected convolutional networks," *CVPR*, 2017.

TABLE I: Performance analysis of binary surface classification

Scene-Id	$k_\mu \times k_\sigma$														
	10×10							20×20							
	Planar			Curved				mIoU	Planar			Curved			
	Precision	Recall	F1	Precision	Recall	F1	Precision		Recall	F1	Precision	Recall	F1	mIoU	
4	0.99	0.95	0.97	0.50	0.98	0.66	0.95	0.99	0.93	0.96	0.38	0.99	0.55	0.93	
20	1.00	0.95	0.97	0.63	1.00	0.67	0.95	0.92	0.96	0.92	0.51	1.00	0.68	0.92	
33	0.97	0.95	0.96	0.74	0.82	0.78	0.92	0.99	0.91	0.95	0.66	0.97	0.79	0.91	
44	0.98	0.96	0.97	0.71	0.89	0.79	0.95	0.99	0.93	0.96	0.61	0.99	0.76	0.93	

TABLE II: Performance analysis of high curvature edge detection, S.B. refers to Shape Back-projection

Scene-Id	Method	$k_\mu \times k_\sigma$	Precision	Recall	F1	Time (S)
4	S.B.	10×10	0.98	0.51	0.67	2.2
	S.B.	20×20	0.94	0.72	0.82	2.2
	[29]	-	0.05	1.00	0.09	2.7
20	S.B.	10×10	0.95	0.63	0.75	2.0
	S.B.	20×20	0.90	0.83	0.86	2.0
	[29]	-	0.05	1.00	0.11	2.5
33	S.B.	10×10	0.87	0.48	0.62	1.5
	S.B.	20×20	0.78	0.75	0.77	1.5
	[29]	-	0.05	1.00	0.09	2.1
44	S.B.	10×10	0.94	0.62	0.75	1.4
	S.B.	20×20	0.84	0.82	0.83	1.4
	[29]	-	0.04	1.00	0.08	2.0
Fig.6a	S.B.	10×10	0.98	0.98	0.98	1.5
	S.B.	20×20	0.42	0.96	0.59	1.5
	[29]	-	0.95	0.98	0.97	1.6

TABLE III: Timing analysis of INAD computations per point

k -NNs	10	100	200	300	400	500
Time (μ S)	4.2	23.1	45.5	67.6	87.5	100.7

TABLE IV: Performance analysis for multi-instance cylinder extraction

Method	Precision	Recall	F1
S.B.	0.66	0.97	0.79
RANSAC [27]	0.16	0.92	0.27

- [18] K. Simonyan and A. Zisserman, "Very deep convolutional networks for large-scale image recognition," *CoRR*, vol. abs/1409.1556, 2014.
- [19] J. Huang and S. You, "Point cloud labeling using 3d convolutional neural network," in *Pattern Recognition (ICPR), 2016 23rd International Conference on*, pp. 2670–2675, IEEE, 2016.
- [20] S. Song, F. Yu, A. Zeng, A. X. Chang, M. Savva, and T. Funkhouser, "Semantic scene completion from a single depth image," in *Computer Vision and Pattern Recognition (CVPR), 2017 IEEE Conference on*, pp. 190–198, IEEE, 2017.
- [21] B. Wu, A. Wan, X. Yue, and K. Keutzer, "Squeezeseg: Convolutional neural nets with recurrent crf for real-time road-object segmentation from 3d lidar point cloud," *arXiv preprint arXiv:1710.07368*, 2017.
- [22] F. Caccavale, G. Giglio, G. Muscio, and F. Pierri, "Adaptive control for uavs equipped with a robotic arm," *IFAC Proceedings Volumes*, vol. 47, no. 3, pp. 11049–11054, 2014.
- [23] T. W. Danko, K. P. Chaney, and P. Y. Oh, "A parallel manipulator for mobile manipulating uavs," in *Technologies for Practical Robot Applications (TePRA), 2015 IEEE International Conference on*, pp. 1–6, IEEE, 2015.
- [24] R. B. Rusu, N. Blodow, and M. Beetz, "Fast point feature histograms (fpfh) for 3d registration," in *Robotics and Automation, 2009. ICRA'09. IEEE International Conference on*, pp. 3212–3217, Citeseer, 2009.
- [25] F. Tombari, S. Salti, and L. Di Stefano, "Unique signatures of histograms for local surface description," in *European conference on computer vision*, pp. 356–369, Springer, 2010.
- [26] F. Tombari and L. Di Stefano, "Object recognition in 3d scenes with occlusions and clutter by hough voting," in *2010 Fourth Pacific-Rim Symposium on Image and Video Technology*, pp. 349–355, IEEE, 2010.
- [27] M. A. Fischler and R. C. Bolles, "Random sample consensus: a paradigm for model fitting with applications to image analysis and automated cartography," *Communications of the ACM*, vol. 24, no. 6, pp. 381–395, 1981.
- [28] R. Garcia, J. Battle, and X. Cufi, "A system to evaluate the accuracy of a visual mosaicking methodology," in *OCEANS, 2001. MTS/IEEE Conference and Exhibition*, vol. 4, pp. 2570–2576, IEEE, 2001.
- [29] D. Bazazian, J. R. Casas, and J. Ruiz-Hidalgo, "Fast and robust edge extraction in unorganized point clouds," in *Digital Image Computing: Techniques and Applications (DICTA), 2015 International Conference on*, pp. 1–8, IEEE, 2015.
- [30] M. J. Swain and D. H. Ballard, "Color indexing," *International journal of computer vision*, vol. 7, no. 1, pp. 11–32, 1991.
- [31] D. Comaniciu and P. Meer, "Robust analysis of feature spaces: color image segmentation," in *Computer Vision and Pattern Recognition, 1997. Proceedings., 1997 IEEE Computer Society Conference on*, pp. 750–755, IEEE, 1997.
- [32] G. R. Bradski, "Computer vision face tracking for use in a perceptual user interface," 1998.
- [33] R. B. Rusu and S. Cousins, "3d is here: Point cloud library (pcl)," in *Robotics and automation (ICRA), 2011 IEEE International Conference on*, pp. 1–4, IEEE, 2011.
- [34] D. Girardeau-Montaut, "Cloud compare—3d point cloud and mesh processing software," *Open Source Project*, 2015.
- [35] M. Everingham, L. Van Gool, C. K. Williams, J. Winn, and A. Zisserman, "The pascal visual object classes (voc) challenge," *International journal of computer vision*, vol. 88, no. 2, pp. 303–338, 2010.
- [36] C. F. Lehnert, A. English, C. McCool, A. W. Tow, and T. Perez, "Autonomous sweet pepper harvesting for protected cropping systems," *IEEE Robotics and Automation Letters*, vol. 2, no. 2, pp. 872–879, 2017.
- [37] N. Mellado, D. Aiger, and N. J. Mitra, "Super 4pcs fast global point-cloud registration via smart indexing," *Computer Graphics Forum*, vol. 33, no. 5, pp. 205–215, 2014.